High-Gain and Low-Driving-Voltage Photodetectors Based on Organolead Triiodide Perovskites

*Rui Dong, Yanjun Fang, Jungseok Chae, Jun Dai, Zhengguo Xiao, Qingfeng Dong, Yongbo Yuan, Andrea Centrone, Xiao Cheng Zeng, and Jinsong Huang**

Weak light sensing in the ultraviolet (UV), visible, and near-infrared (NIR) range has a wide variety of applications in fields that are of importance to both industry and defense as well as scientific research.[1,2] Solution-processable optoelectronic materials, such as organic materials, nanomaterials, and nanocomposites, have shown promise as active layers in large-area, low-cost photodetectors, because they frequently provide photoconductive gain (defined as the number of charges flowing through an external circuit per incident photon). However, further improvement of their detection performance is hindered by their poor charge carrier mobilities.[3,4] Organometal trihalide perovskites (OTPs) (with the molecular structure $CH_3NH_3PbX_3$, where X = Cl, Br, I, or a mixed halide) are a new family of optoelectronic materials that combine good solution processability with high Hall mobilities, i.e., comparable to that of crystalline silicon. OTP-based photodetectors potentially mark a paradigm shift in the engineering of low-cost, yet high-performance photodetectors. In contrast to silicon, solution-processed OTPs are direct bandgap semiconductors with very large absorption coefficients of up to $\approx 10^5$ cm^{-1} in the UV–vis range.[5] OTP solar cells show promise for competing with commercial silicon solar cells because they achieve remarkably high power conversion efficiencies of ≈15–18% within only four years of development.[5–8] More and more experimental evidence suggests that defects/traps may be abundant in the OTP layer, either within the bulk or at the surface.[7–11] Although these trap states are detrimental to the performance of photovoltaic devices, we show in this paper that it is possible to exploit traps to boost the performance of perovskite photodetectors with an ingenious device design.

Dr. R. Dong, Dr. Y. Fang, Z. Xiao, Dr. Q. Dong, Dr. Y. Yuan, Prof. X. C. Zeng, Prof. J. Huang
Department of Mechanical and Materials Engineering
University of Nebraska-Lincoln
Lincoln, NE 68588, USA
E-mail: jhuang2@unl.edu

Dr. J. Chae, Dr. A. Centrone
Center for Nanoscale Science and Technology
National Institute of Standards and Technology
100 Bureau Drive, Gaithersburg, MD 20899, USA

Dr. J. Chae
Maryland Nanocenter
University of Maryland
College Park, MD 20742, USA

Dr. J. Dai, Prof. X. C. Zeng
Department of Chemistry
University of Nebraska-Lincoln
Lincoln, NE 68588, USA

DOI: 10.1002/adma.201405116

In this paper, we describe the fabrication and characterization of solution-processed $CH_3NH_3PbI_3$ photodetectors that combine a high photoconductive gain with a broad spectral response, ranging from the UV to the NIR. Benefitting from the trapped-hole-induced electron injection, the $CH_3NH_3PbI_3$ photodetector works as a photodiode in the dark and shows large photoconductive gain under illumination. The maximum device gain reached 489 ± 6 at a very low driving voltage of –1 V.

The devices studied here have a layered inverted structure (**Figure 1**a) where indium tin oxide (ITO) is the cathode, $CH_3NH_3PbI_3$ is the active layer, 4,4′-bis[(p-trichlorosilylpropylphenyl)phenylamino]-biphenyl (TPD–Si_2) serves as the hole transporting/electron blocking layer, molybdenum trioxide (MoO_3) is used for anode work function modification, and silver (Ag) as the anode. The $CH_3NH_3PbI_3$ layers were prepared by thermal-annealing induced interdiffusion of the two perovskite precursors (PbI_2, CH_3NH_3I) by way of a method that has recently been developed in our group to fabricate very efficient solar cells with high yield.[8] In short, lead iodide (PbI_2) films were deposited first on ITO/glass substrates by spin-coating. A second layer consisting of methylammonium iodide (CH_3NH_3I) (hereafter MAI) was then spin-coated on top of the dried PbI_2 film, followed by thermal annealing at 105 °C for 60 min. Scanning electron microscopy (SEM) measurements (Figure S1, Supporting Information) showed that the interdiffusion method allows the preparation of $CH_3NH_3PbI_3$ films on ITO that are continuous and uniform, which is particularly important for obtaining leakage-free photodetectors. The absorption curve in Figure 1b shows that the $CH_3NH_3PbI_3$ films have a broad absorption spectrum that ranges from 300 nm (UV) to 800 nm (NIR).

The photo- and dark-current densities–voltage (*J*–*V*) curves of $CH_3NH_3PbI_3$ photodetectors (Figure 1c) show a transition from a diode-rectifying behavior in the dark, to photoconduction under illumination. Under illumination, both the forward and the reverse bias currents increased dramatically, with the reverse bias current increasing more sharply than the forward bias current. The rectifying effect completely disappeared, and an ohmic conduction behavior (symmetrical photocurrent with respect to the *y*-axis) was observed when exposing the device to white light irradiation (10 mW cm^{-2}). For comparison, the *J*–*V* curve of a high performance solar cell (where exactly the same $CH_3NH_3PbI_3$ fabrication procedure was applied) with almost 100% external quantum efficiency under the same light intensity is also shown in Figure 1c. The reference photovoltaic (PV) device has a structure of ITO/PEDOT:PSS/$MAPbI_3$/[6,6]-phenyl-C_{61}-butyric acid methyl ester (PCBM) (20 nm)/C_{60} (20 nm)/2,9-dimethyl-4,7-diphenyl-1,10-phenanthroline (BCP) (8 nm)/aluminium (Al) (100 nm).[8] Although

ADVANCED MATERIALS
www.advmat.de

www.MaterialsViews.com

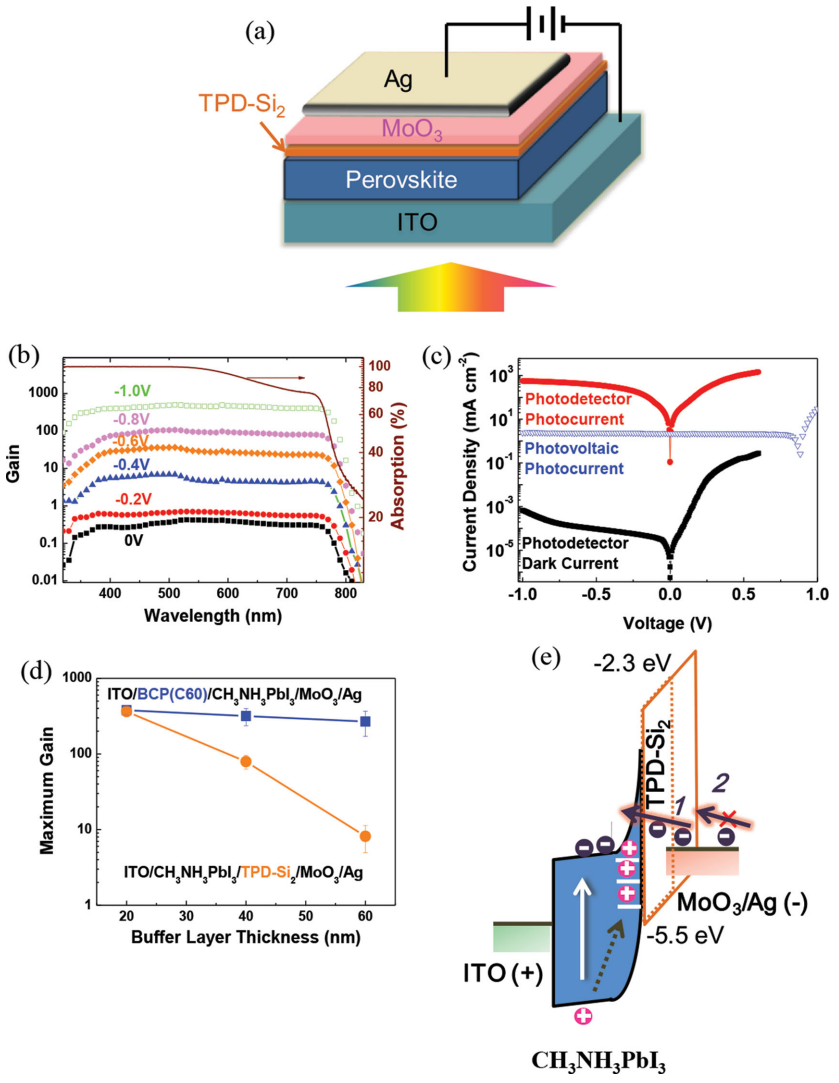

Figure 1. a) Device structure of the $CH_3NH_3PbI_3$ photodetector. b) Absorption spectrum (solid line) of the $CH_3NH_3PbI_3$ films and wavelength-dependent gain (solid lines with symbols) of the $CH_3NH_3PbI_3$ devices under reverse biases between 0 to –1 V. c) Photo- and dark-current-density–voltage (*J*–*V*) curves of the $CH_3NH_3PbI_3$ device. The reference PV device has a structure of ITO/PEDOT:PSS/$MAPbI_3$/PCBM/C_{60}/BCP/Al. d) The dependence of maximum gain values of the $CH_3NH_3PbI_3$ photodetectors on the thickness of single-carrier blocking layers. e) Energy diagram of the $CH_3NH_3PbI_3$ photodetector at reverse bias under illumination.

the photodetector exhibits a similar structure to that of the reference PV device, the PCBM and C_{60} passivation layers were intentionally omitted to leave surface trap states in the photodetectors because fullerenes can passivate most of the charge traps. The photocurrent biased at –1 V is more than 100 times larger for the $CH_3NH_3PbI_3$ photodetector device than for the photovoltaic device, highlighting the large gain provided by the perovskite photodetector. The device's peak responsivity (R), defined by the ratio of the photocurrent density at –1 V and the incident white light intensity, was calculated to be 56 ± 2 A W^{-1}. The uncertainties through the manuscript represent a single standard deviation in the measurements on nominally identical devices.

Incident photon-to-current efficiency (IPCE) measurements can provide the device photoconductor gain directly by providing the number of charges flowing through an external circuit per incident photon. An IPCE value of 100% corresponds to a photodetector gain value of 1. It should be noted that, in absence of a charge multiplication mechanism,[2,12] the IPCEs measured at 0 V bias are generally below 100% for photovoltaic devices, because all the charges that flow through the external circuit are photogenerated. In contrast, a photoconductor can have IPCEs above 100% because, in addition to the photogenerated charges, charges are also injected by the electrodes under an applied bias. The resulting photovoltaic gain can be much larger than 1, because the injected charges can be significantly higher than the photogenerated charges. IPCE measurements were carried out at reverse biases between 0 and –1 V with stepwise increases of –0.2 V. As shown in Figure 1b, the IPCE curves agree well with the profile derived from the absorption curve. The gain of the $CH_3NH_3PbI_3$ device increased as a function of the reverse bias from 0.3 at zero bias and exceeded 1 at –0.4 V. At –1 V, the gains reached 299 ± 6, 475 ± 6, and 405 ± 6 at wavelengths of 350, 530, and 740 nm, respectively. The device's wavelength-dependent responsivity can be calculated from the wavelength dependent gain by:

$$R(\lambda) = \frac{\text{Gain}(\lambda)}{E_{h\nu}} \quad (1)$$

where $E_{h\nu}$ is the energy of the incident photon (in eV). We obtained device responsivities of 84, 203, and 242 A W^{-1}, at the three wavelengths (350, 530, and 740 nm), respectively.

The large gain measured provides evidence that perovskite devices work as photoconductors under illumination. A photoconductive gain is obtained when a photon-generated transport charge can travel through the circuit multiple times before recombination, because the charge recombination lifetime (τ_r) is larger than the charge transit time (τ_t), which is the drift time that is needed for charges to travel from one electrode to the opposite electrode under the applied field; the photoconductive gain can then be determined by calculating the ratio $\frac{\tau_r}{\tau_t}$.[13] In contrast to a rectifying Schottky junction in a photodiode, a photoconductor requires a semiconductor–metal ohmic contact to supply sufficient circulating charge. In the dark there are large energy barriers for electron injection from the MoO_3/Ag electrode to the OTP layer, and for hole injection from the ITO to the OTP layer, which explains the rectification behavior in the dark. One of these two contacts must change from a Schottky junction to an ohmic contact when

DOI: 10.1002/adma.201405116

the device is illuminated. To explain this behavior, we hypothesize that one type of trapped charges in the $CH_3NH_3PbI_3$ active layer induces band bending in the perovskite layer close to one of the electrodes, thus reducing the Schottky junction thickness, and allowing the injection of the opposite charges under reverse bias.[4,14] Either the anode or the cathode interface could in principle undergo such a transition when illuminated. To identify which contact turns to ohmic under illumination, single-carrier blocking layers were inserted at both interfaces between the OTP layer and the anode/cathode. It is expected that by inserting a thick charge transport buffer layer the transition from Schottky junction to ohmic contact will be hindered, preventing charge tunneling from the electrode and eliminating the gain. Electron transport layers consisting of C_{60} or 2,9-dimethyl-4,7-diphenyl-1,10-phenanthroline (BCP) were inserted between ITO and OTP, and an hole transport layer (TPD–Si_2) was inserted between OTP and MoO_3/Ag electrode. Almost no change in the maximum gain values was observed by increasing the thickness of BCP or C_{60} from 20 to 60 nm (Figure 1d). On the contrary, the maximum gain values were reduced dramatically by increasing the thickness of the TPD–Si_2 layer, as shown in Figure 1d. This suggests that the ohmic contact is formed at the top interface between OTP and the MoO_3/Ag electrode, and that hole-traps should be abundant on the top surface of the perovskite films (Figure 1e).

A large density of trap states in perovskite films was observed in a few experimental studies,[9,10] despite the fact that first-principles density-functional theory (DFT) calculations suggested that point defects in $MAPbI_3$ (MA = CH_3NH_3) do not generate trap states within the material bandgap.[11] Previously we used thermal admittance spectroscopy (TAS) analysis to reveal trap densities as large as 10^{18} or 10^{19} m^{-3} in the pristine $MAPbI_3$ films.[7] This discrepancy may be reconciled if a large density of traps is confined at the top surface of the perovskite film whereas the trap density in the film bulk remains very small. This occurrence may be explained by decomposition at the perovskite surface upon thermal annealing. Compared to the traditional inorganic semiconductors, the hybrid OTPs such as $MAPbI_3$ are less thermally stable, which can be explained by the low dissociation energy of $MAPbI_3$.[15] The $MAPbI_3$ decomposition temperature is 300 °C,[16] but decomposition at surfaces or grain boundaries may occur at much lower temperatures. Here, we have applied the photothermal induced resonance (PTIR) technique to study the surface decomposition of perovskite films. PTIR is a novel technique that combines the lateral resolution of atomic force microscopy (AFM) with the chemical specificity of IR spectroscopy, thus enabling the acquisition of IR absorption spectra and maps with nanoscale resolution.[17–19] PTIR uses total internal reflection to illuminate the sample and an AFM tip in contact mode as a near-field detector to transduce the thermal expansion induced by light absorption in the sample for gathering local chemical information (**Figure 2**a). Notably, for thin samples (<1 μm)[18] the PTIR signal is proportional to the sample absorbed energy. For this study we built a custom enclosure that allows recording PTIR data under a nitrogen flow, and a temperature stage that allows annealing of the sample in situ. A perovskite film was spun on an IR transparent prism, and measured as prepared and after annealing at 140 °C, which is close to the device annealing temperature, for 10, 30, and 60 min. Since the vibrational modes involving Pb occur at a much lower frequency than the PTIR spectral range,[19] the spectra and images presented here essentially probe the MAI component of the perovskite material. The surface topography map and PTIR chemical map at 1468 cm^{-1} (corresponding to the CH_3 anti-symmetric stretching of the methylammonium ion) of the as-prepared $MAPbI_3$ film are shown in Figure 2c and 2d, respectively, and were used as reference. After annealing for 10 min, the surface topography map (Figure 2e) shows either a minimal or no obvious change with respect to the as-prepared film; however, the PTIR chemical map (Figure 2f) shows that distinct striations appear. Representative PTIR spectra (Figure 2b) recorded from grains with striations, as a function of annealing time (0 min (as-prepared), and 10, 30, and 60 min) of the $MAPbI_3$ film show an obvious suppression of the CH_3 anti-symmetric stretching of the methyl ammonium ion at 1468 cm^{-1}. Since the PTIR intensity refers to the MAI content, and since the PTIR signal is proportional to the absorbed energy, a reduction of the MAI content in the $MAPbI_3$ film is expected upon annealing, which provides direct evidence of surface decomposition of $MAPbI_3$. We attribute the striations in the PTIR image to the onset of MAI loss, which should leave a rich PbI_2 film surface. Since Pb is not volatile, we speculate that the surface decomposition leaves a large density of Pb^{2+} clusters on the film surface, which are the origin of the charge traps in the photodetector devices. For longer annealing times the surface decomposition is more obvious and leads to an increase in surface roughness and heterogeneity in the PTIR images. An electron paramagnetic resonance study by Shkrob and Marin[10] showed that Pb^{2+} clusters act indeed as hole traps, which is also supported by our calculations (see below).

The first-principles calculations were performed within the framework of the density functional theory.[20] Ion-electron interation was treated with the projector augment waves (PAW) approximation.[21] The optB88-vdW functional[22] was adopted for the exchange-correlation potential, which has been shown to provide the best agreement between the computed structural parameters and the experimental crystallographic parameters of $MAPbI_3$.[23] Surfaces cleaved along the [001] direction with PbI_2- and MAI-termination were constructed where the bottom Pb atoms were passivated by H atoms. To simplify the calculation, we considered the simplest Pb cluster, i.e., a Pb dimer, which was added onto a 2×2 PbI_2-terminated surface to examine the possible origin of the trap states, as shown in **Figure 3**a. The computed electronic band structures and density of states (DOS) of PbI_2-terminated surface with a Pb dimer (per supercell) are illustrated in Figure 3b and 3c, and show that the Pb^{2+} dimers cause both hole and electron traps. We note that the electron traps were not evident in our devices as well as in other solar cells devices, which is attributed to the passivation effect of the conducting polymer coating the perovskite surface or to electrons repulsion from the surface due to the applied electric field. The trap passivation of the TPD–Si_2 layer has been demonstrated in organic light-emitting diodes, because of its ability of terminating surface dangling bonds, eliminating adsorbed water and interacting with oxide electrode surfaces.[24] Nevertheless, our DFT calculation revealed the origin of the hole traps and their correlation with small-sized Pb clusters.

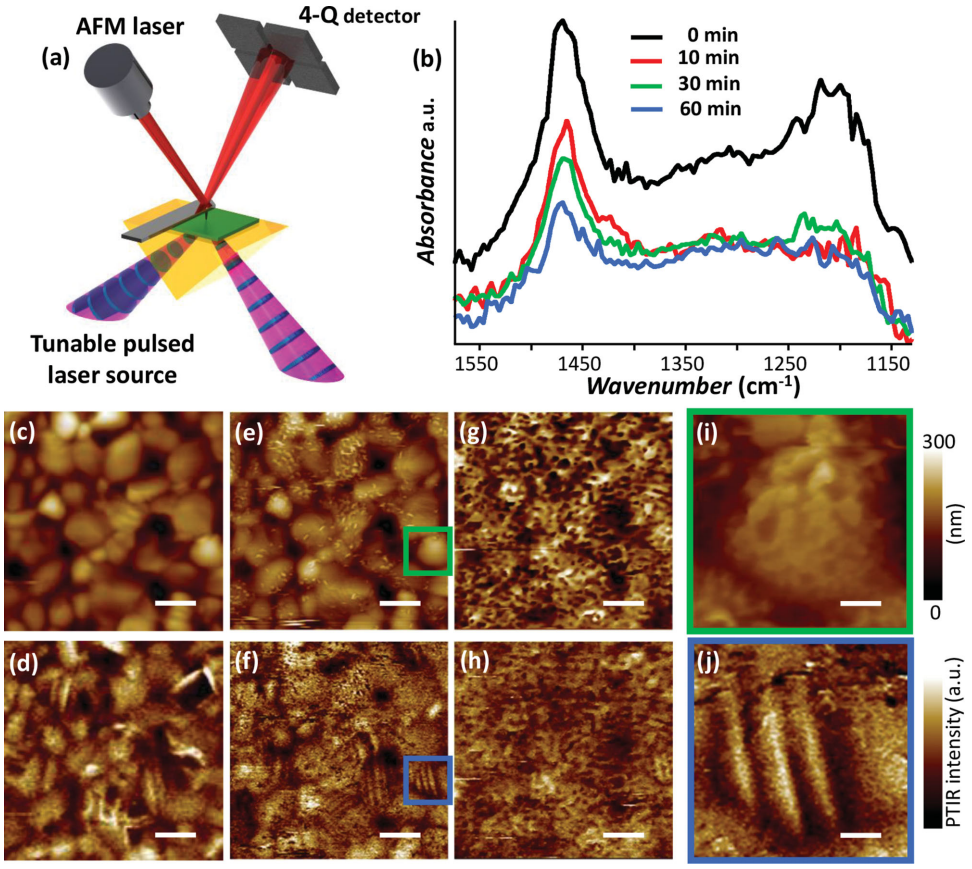

Figure 2. a) Schematic of the PTIR experimental setup. b) PTIR spectra as a function of annealing time. c–h) Height and PTIR images of the same sample area before annealing (c,d), and after annealing for 10 min (e,f) or 60 min (g,h). All the scale bars in panels c–h are 1 μm. i,j) High-resolution height and PTIR images of the sample area marked by the boxes in Figure 3e and 3f respectively, obtained after 30 min of annealing. The scale bars in panels (i,j) are 200 nm. All PTIR images were recorded at 1468 cm^{-1} corresponding to the CH_3 antisymmetric stretching of the methylammonium ion.

Having identified the nature of charge traps on the OTP surface, we can modulate the density of hole traps (i.e., the device gain) by varying the composition of the perovskite films. Here, $MAPbI_3$ layers were optimized for the best device performance by evaluating the precursor ratio (PbI_2/MAI) during the film formation process. The maximum gain of the $MAPbI_3$ photodetectors was strongly affected by the PbI_2/MAI weight ratio (**Figure 4**a), and peaked at 600 mg mL^{-1} for PbI_2 with a fixed MAI concentration (43 mg mL^{-1}). Table S1 in the Supporting Information provides the $MAPbI_3$ layer thickness obtained by varying the PbI_2 concentration from 400 to 800 mg mL^{-1} and a fixed MAI concentration of 43 mg mL^{-1}. The maximum gain of the $MAPbI_3$ photodetectors was also influenced by the $MAPbI_3$ layer thickness (Table S1, Supporting Information), as was the maximum for a $MAPbI_3$ thickness between 360 and 410 nm. In principle, a large thickness can result in smaller photo responses, but the challenge is the difficulty of separating the thickness change from the composition change since both of them change in our films. The concentrations that gave the best device performance in our study differs from that used to realize $MAPbI_3$ solar cells (400 mg mL^{-1} for PbI_2 and 45 mg mL^{-1} for MAI),[8] even if exactly the same fabrication procedure was applied. This suggests that a PbI_2 richer composition favors a larger density of hole traps on the top surface, reinforcing our findings that Pb^{2+} cations act as hole traps.

The temporal response of the photocurrent was evaluated by using a 532 nm laser with a light intensity of around 0.2 mW cm^{-2} modulated with a chopper at 3000 Hz (Figure 4b). The device shows a short rise time of 10 ± 0.8 μs (from 10% to 90% of its peak value), and a biexponential photocurrent decay with time constant of 5.7 ± 1.0 μs and 41 ± 3.2 μs for the fast and slow component, respectively. Both the rise time and decay time should be limited by the charge trapping/detrapping process because all other processes, such as charge generation and carrier drifting, should be much faster. The photocurrent multiexponential decay indicates the existence of two recombination channels for the trapped holes, probably related to hole traps with different trap depths. The gain (G) of the $MAPbI_3$ photodetector can also be calculated by the measured carrier recombination lifetime and transit time, and is determined by:

$$G = \frac{\tau_{\text{lifetime}}}{\tau_{\text{transit time}}} = \frac{\tau_{\text{lifetime}}}{d^2/\mu V} \quad (2)$$

where d is the device thickness, V is the applied bias, and μ is the carrier mobility in the direction across the film. Here, the carrier recombination lifetime is 5.7 μs, $V = 0.75$ V, $d = 390$ nm,

Adv. Mater. 2015,
DOI: 10.1002/adma.201405116

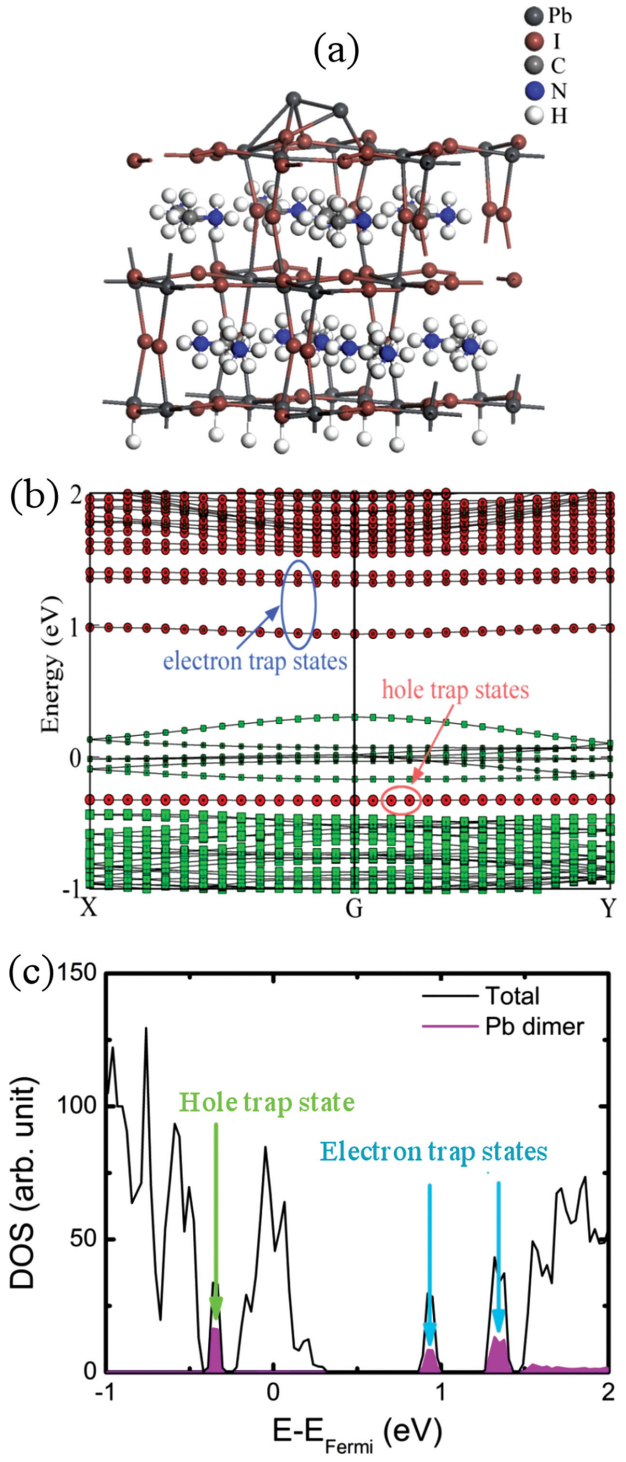

Figure 3. a) Schematic view of Pb dimer on a PbI_2-terminated surface. b) The computed electronic band structures, where the red and green spheres denote the contribution from Pb and I atoms, respectively. c) The computed density of states curves, where the partial density of states (pDOS) from the Pb dimer is highlighted in pink.

$\mu \approx 1.5 \times 10^{-2}$ cm^2 V^{-1} s^{-1},[8] leading to a calculated photoconductor gain of 43 ± 7.5, which is close to the measured gain by the IPCE method at the same bias.

A desirable characteristic for a photodetector is to have an identical responsivity over a wide range of light intensity, which is known as the linear dynamic range (LDR). The LDR was measured by recording the photocurrent of the $CH_3NH_3PbI_3$ photodetector under 532 nm laser illumination with the light intensity varying from 6.9×10^{-9} to 3.6 mW cm^{-2} (Figure 4c). The $CH_3NH_3PbI_3$ photodetector exhibited a linear response with the light intensity ranging from 6.9×10^{-9} to 0.23 mW cm^{-2}, corresponding to a LDR of 85 dB. Under stronger illumination, the device photocurrent deviated from the linear relationship with a lower output, which explains the discrepancy of the responsivities obtained with IPCE and photocurrent, because they were measured with different light intensities.

The noise equivalent power (NEP) represents the weakest light intensity measurable by a photodetector or the light intensity threshold below which the photocurrent can no longer be distinguished from the noise current. The devices' NEP was directly measured for the first time here by measuring the signal current together with the noise current under various light intensities. A chopper modulated 532 nm laser (35 Hz) was used to illuminate the device, and the frequency-dependent photocurrent signal, under a reverse bias of –0.7 V, was recorded by a FFT spectrum analyzer. As shown in Figure 4d, a peak at 35 Hz was observed with intensity decreasing as a function of the incident light intensity, in addition to the $1/f$ noise background. The lowest detectable light intensity (at 35 Hz) was ca. 6.2 pW cm^{-2}, or 0.37 pW for a device area of 6 mm^2. The NEP can also be calculated by:

$$\mathrm{NEP} = \frac{\overline{I_n^2}^{1/2}}{R} \tag{3}$$

where $\overline{I_n^2}^{1/2}$ is the total noise current and R is the responsivity. The NEP was calculated to be 0.18 pW, which is smaller but close to the measured NEP and is also close to the LDR measurement (0.4 pW). The excellent weak light detection capability of the perovskite photodetector benefits from the low noise enabled by the crosslinked TPD–Si_2 buffer layer, as well as the high gain due to the charge injection induced by the interfacial traps.

In addition to reducing the noise current, the crosslinked TPD–Si_2 electron blocking layer also improves the device stability by encapsulating the perovskite active layer. No discernable degradation of gain was observed after storing the as-prepared OTP photodetector in air at room temperature for more than three weeks (Figure 4e), indicating that the crosslinked hydrophobic TPD–Si_2 layer effectively prevents the permeation of moisture to the perovskite layer. Photocurrent hysteresis provides a challenge for measuring efficiency accurately in perovskite photovoltaic devices.[25] For a photodetector, a reproducible photocurrent output is needed for determining the light intensity accurately. We measured the photocurrent at low light intensity, which is of greater interest for practical applications. The photocurrent output of the OTP photodetector was recorded by increasing/decreasing the irradiation intensity repeatedly (Figure 4f). The photodetectors showed excellent reproducibility for the detection of weak light while no obvious hysteresis was discerned.

In summary, we report a highly sensitive OTP-based photodetector with a broadband response ranging from the

ADVANCED MATERIALS
www.advmat.de

www.MaterialsViews.com

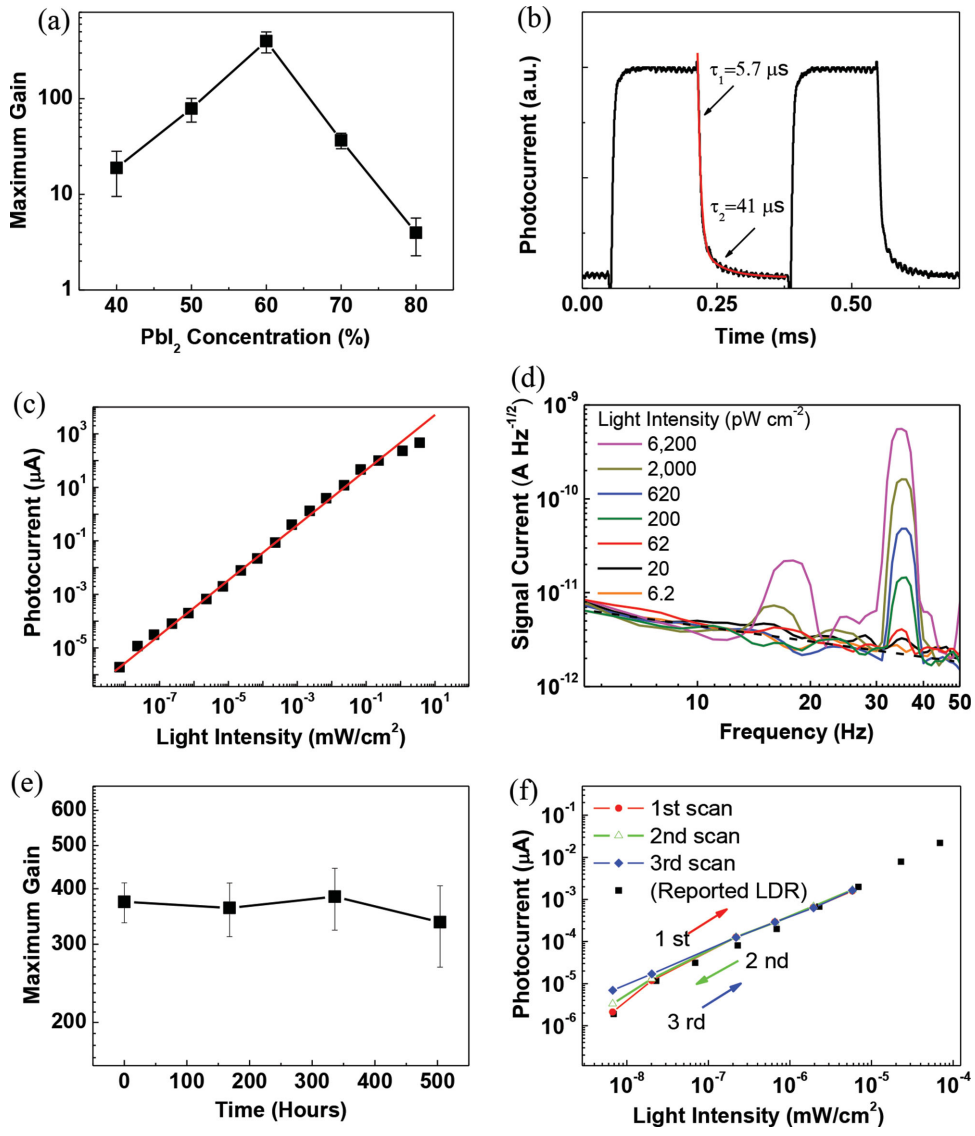

Figure 4. a) Maximum gain of the $CH_3NH_3PbI_3$ photodetectors as a function of the PbI_2/MAI relative mass fraction. b) Transient photocurrent of the $CH_3NH_3PbI_3$ photodetector. c) Dynamic response of the photodetector. d) The noise current spectrum of the photodetector measured with various light intensities (the dashed line is the $1/f$ noise background). e) The gain of the OTP photodetector measured in air at room temperature over three weeks. f) Weak light detection of the $CH_3NH_3PbI_3$ photodetector after three circles of light intensity sweeping.

UV to the NIR. The $CH_3NH_3PbI_3$ photodetectors showed a very high responsivity of 242 A W^{-1} at low bias (–1 V). The hole traps caused by large concentration of Pb^{2+} cations in the perovskite film top surface is critical for achieving high gain in these devices. The extremely low bias needed for the OTP photodetectors allows powering them with miniature button batteries and/or compact integration with existing low voltage circuits.

Supporting Information

Supporting Information is available from the Wiley Online Library or from the author.

Acknowledgements

R.D. and Y.F. contributed equally to this work. This work was supported by the Defense Threat Reduction Agency (Award No. HDTRA1–14–1–0030, HDTRA1-10-1-0098), the Office of Naval Research (ONR, Award No. N000141210556), the National Science of Foundation (Award No. CMM-1265834) and the Nebraska Public Power District through the Nebraska Center for Energy Sciences Research.

Received: November 7, 2014
Revised: December 9, 2014
Published online:

[1] X. Gong, M. Tong, Y. Xia, W. Cai, J. S. Moon, Y. Cao, G. Yu, C.-L. Shieh, B. Nilsson, A. J. Heeger, *Science* **2009**, *325*, 1665.
[2] G. Konstantatos, E. H. Sargent, *Nat. Nanotechnol.* **2010**, *5*, 391.

DOI: 10.1002/adma.201405116

[3] a) G. Konstantatos, I. Howard, A. Fischer, S. Hoogland, J. Clifford, E. Klem, L. Levina, E. H. Sargent, *Nature* **2006**, *442*, 180; b) H.-Y. Chen, M. K. F. Lo, G. Yang, H. G. Monbouquette, Y. Yang, *Nat. Nanotechnol.* **2008**, *3*, 543.
[4] R. Dong, C. Bi, Q. Dong, F. Guo, Y. Yuan, Y. Fang, Z. Xiao, J. Huang, *Adv. Opt. Mater.* **2014**, *2*, 549.
[5] M. A. Green, A. Ho-Baillie, H. J. Snaith, *Nat. Photonics* **2014**, *8*, 506.
[6] a) A. Kojima, K. Teshima, Y. Shirai, T. Miyasaka, *J. Am. Chem. Soc.* **2009**, *131*, 6050; b) J. Burschka, N. Pellet, S.-J. Moon, R. Humphry-Baker, P. Gao, M. K. Nazeeruddin, M. Gratzel, *Nature* **2013**, *499*, 316; c) M. Liu, M. B. Johnston, H. J. Snaith, *Nature* **2013**, *501*, 395; d) H. Zhou, Q. Chen, G. Li, S. Luo, T.-b. Song, H.-S. Duan, Z. Hong, J. You, Y. Liu, Y. Yang, *Science* **2014**, *345*, 542.
[7] Q. Wang, Y. Shao, Q. Dong, Z. Xiao, Y. Yuan, J. Huang, *Energy Environ. Sci.* **2014**, *7*, 2359.
[8] Z. Xiao, C. Bi, Y. Shao, Q. Dong, Q. Wang, Y. Yuan, C. Wang, Y. Gao, J. Huang, *Energy Environ. Sci.* **2014**, *7*, 2619.
[9] J. Kim, S.-H. Lee, J. H. Lee, K.-H. Hong, *J. Phys. Chem. Lett.* **2014**, *5*, 1312.
[10] I. A. Shkrob, T. W. Marin, *J. Phys. Chem. Lett.* **2014**, *5*, 1066.
[11] W.-J. Yin, T. Shi, Y. Yan, *Appl. Phys. Lett.* **2014**, *104*, 063903.
[12] K.-J. Baeg, M. Binda, D. Natali, M. Caironi, Y.-Y. Noh, *Adv. Mater.* **2013**, *25*, 4267.
[13] a) K. K. Ng, S. M. Sze, *Physics of Semiconductor Devices*, John Wiley and Sons, Hoboken, NJ, USA **2007**; b) J. M. Liu, *Photonics Devices*, Cambridge University Press, New York **2005**.
[14] F. Guo, B. Yang, Y. Yuan, Z. Xiao, Q. Dong, Y. Bi, J. Huang, *Nat. Nanotechnol.* **2012**, *7*, 798.
[15] a) A. Dualeh, N. Tétreault, T. Moehl, P. Gao, M. K. Nazeeruddin, M. Grätzel, *Adv. Funct. Mater.* **2014**, *24*, 3250; b) C. Bi, Y. Shao, Y. Yuan, Z. Xiao, C. Wang, Y. Gao, J. Huang, *J. Mater. Chem. A* **2014**, *2*, 18508.
[16] T. Baikie, Y. Fang, J. M. Kadro, M. Schreyer, F. Wei, S. G. Mhaisalkar, M. Graetzel, T. J. White, *J. Mater. Chem. A* **2013**, *1*, 5628.
[17] a) A. M. Katzenmeyer, J. Canivet, G. Holland, D. Farrusseng, A. Centrone, *Angew. Chem. Int. Ed.* **2014**, *53*, 2852; b) A. Dazzi, R. Prazeres, F. Glotin, J. M. Ortega, *Opt. Lett.* **2005**, *30*, 2388.
[18] B. Lahiri, G. Holland, A. Centrone, *Small* **2013**, *9*, 488.
[19] A. M. Katzenmeyer, V. Aksyuk, A. Centrone, *Anal. Chem.* **2013**, *85*, 1972.
[20] G. Kresse, J. Furthmüller, *Phys. Rev. B* **1996**, *54*, 11169.
[21] P. E. Blöchl, *Phys. Rev. B* **1994**, *50*, 17953.
[22] a) M. Dion, H. Rydberg, E. Schröder, D. C. Langreth, B. I. Lundqvist, *Phys. Rev. Lett.* **2004**, *92*, 246401; b) J. Klimeš, D. R. Bowler, A. Michaelides, *Phys. Rev. B* **2011**, *83*, 195131.
[23] E. Menéndez-Proupin, P. Palacios, P. Wahnón, J. C. Conesa, *Phys. Rev. B* **2014**, *90*, 045207.
[24] J. Cui, Q. Huang, J. C. G. Veinot, H. Yan, Q. Wang, G. R. Hutchison, A. G. Richter, G. Evmenenko, P. Dutta, T. J. Marks, *Langmuir* **2002**, *18*, 9958.
[25] H. J. Snaith, A. Abate, J. M. Ball, G. E. Eperon, T. Leijtens, N. K. Noel, S. D. Stranks, J. T.-W. Wang, K. Wojciechowski, W. Zhang, *J. Phys. Chem. Lett.* **2014**, *5*, 1511.